Nanoscale

Molecular Quantum Interference Effects on Thermopower in Hybrid 2-Dimensional Monolayers

Journal:	*Nanoscale*
Manuscript ID	NR-ART-03-2022-001731
Article Type:	Paper
Date Submitted by the Author:	29-Mar-2022
Complete List of Authors:	Ghomian, Taher; Marshall University, Kizilkaya, Orhan; Louisiana State University, CAMD Domulevicz, Lucas; University of California Davis Hihath, Joshua; University of California, Davis, Electrical and Computer Engineering

Molecular Quantum Interference Effects on Thermopower in Hybrid 2-Dimensional Monolayers

Taher Ghomian[1,2], Orhan Kizilkaya[3], Lucas Kyle Domulevicz[1], and Joshua Hihath[1]

[1]Department of Electrical and Computer Engineering, University of California, Davis, CA 95616, USA
[2]Department of Computer Science and Electrical Engineering, Marshall University, Huntington, WV 25755, USA
[3]Center for Advanced Microstructures and Devices, Louisiana State University, Baton Rouge, LA 70803, USA

Abstract

Quantum interference effects in single-molecule devices can significantly enhance the thermoelectric properties of these devices. However, single-molecule systems have limited utility for power conversion. In this work, we study the effects of destructive quantum interference in molecular junctions on the thermoelectric properties of hybrid, 2-dimensional molecule-nanoparticle monolayers. We study two isomers of Benzenedithiol molecules, with either a para or meta configuration for the thiol groups, as molecular interlinkers between gold nanoparticles in the structure. The asymmetrical structure in the meta configuration significantly improves the Seebeck coefficient and power factor over the para configuration. These results suggest that thermoelectric performance of engineered, nanostructured material can be enhanced by harnessing quantum interference effects in the substituent components.

Keywords:

Thermoelectric; nanomaterials; quantum interference; nanoparticles; superlattice; Seebeck coefficient; power factor; Nanoparticle array (NPA).

Introduction

Thermoelectric devices generate a voltage in response to an applied temperature gradient. This effect was discovered by Thomas Seebeck in 1821 [1]. Today, thermoelectric generators (TEGs) are increasingly being used to convert wasted heat energy into electricity [2-7]. However, they have not garnered wide-spread use because of the generally low-efficiency of these systems, the efficiency of thermoelectric generators is described in terms of figure of merit (ZT) and given by [8]:

$$ZT = \frac{\sigma S^2 T}{\kappa} \quad (1)$$

where σ is electric conductivity, S is the Seebeck coefficient, T is the temperature, and κ is the thermal conductivity.

Over the last 2 decades, much of the work in thermoelectric systems has focused on nanostructured materials, which provide opportunities for optimizing both the electrical conductivity and thermal conductivity of the system beyond the limitations of bulk materials [9-11]. Quantum confinement phenomena in nanomaterials can enhance the Seebeck coefficient and surface and interface effects in nanomaterials can be used to enhance the scattering of phonons that contribute strongly to the thermal conductivity while attempting to maintain electrical conductivity [12-14].

In the hybrid nanostructured systems examined here, organic linkers on the surface of the nanoparticles play an important role in the thermoelectric performance of the

composite system through three effects. First, they limit phonon mode propagation through the lattice due to the large mismatch in phonon modes between the molecules and the nanoparticles [4, 13, 15-20]. Second, they play an important role in the electrical conductivity of the system [21, 22]. Often, molecules act as simple tunneling barriers for charges moving between the nanoparticles. However, these barriers can be tailored to improve the electronic coupling between nanoparticles, and thus improve the electrical conductivity [23-25]. Importantly, electrical conductivity in organic molecules is not simply proportional to the length of the molecules but is a complex function of the electronic structure [26-34]. As such, two molecules with similar atomic structure may present completely different conductance behavior because of the change in electronic states of the molecule and the molecule-nanoparticle interaction.

The third effect that molecules have on the thermoelectric performance relates to the Seebeck coefficient. The Seebeck coefficient in nanoparticle array (NPA) is determined by the slope of the transport probability of the charge carrier through the molecular junction near the Fermi level (Figure 1) [8, 35].

$$S_{NPA} \approx -\frac{\pi^2 k_B^2 T}{3e} \frac{\partial ln\mathcal{T}(E)}{\partial E}\Big|_{E=E_F} \quad (2)$$

where k_B is Boltzmann's constant, e is the elementary charge, E is the energy of the charge carrier, E_F is the Fermi level, and $\mathcal{T}(E)$ is the transmission function. Thus, by tuning the transmission function, one can improve both the conductance and the Seebeck coefficient simultaneously in molecular transport-controlled systems.

One potential method of engineering the slope of the transmission function is to take advantage of destructive quantum interference (DQI) in the molecular junctions to create sharp anti-resonant features in the transmission function, which can result in

substantial increases in slope throughout the transmission function, and improve the Seebeck coefficient almost regardless of the position of the Fermi energy [36-42]. Recent advances in theoretical models focusing on the conductance behavior of common molecules such as benzene-based molecules have yielded good agreement with experimental results and additional insights into the transport behavior [36-39, 43-47]. In addition, improvement in nanofabrication techniques now provide a suitable platform for the realization of devices based on molecule-nanoparticle junctions [26, 48-50]. Since computational studies show that significant improvement in thermoelectric performance can be achieved in materials with quantum interference effects [21, 29, 51-54], and recent experimental studies have verified this at the single-molecule level [52]. we here aim to leverage these properties in 2D systems to explore the translation of enhanced thermoelectric properties from single-molecule systems to larger scales.

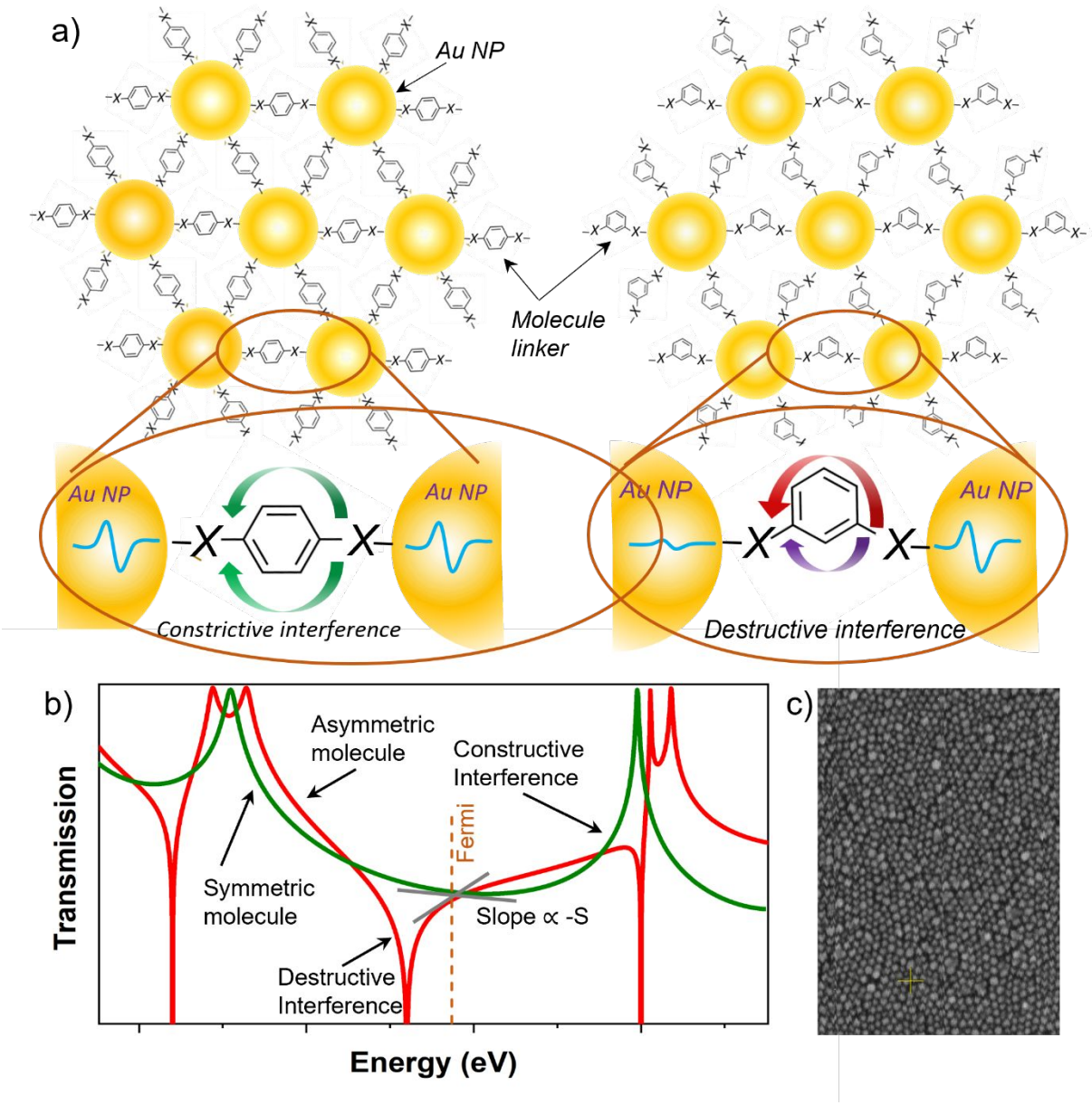

Figure 1. (a) Schematic overview of the gold nanoparticles array with molecule linker to examine the effects of quantum interference at large scales for both symmetric (left figure) and asymmetric (right figure) molecule linkers. (b) Schematic overview of the effect of DQI on the thermoelectric properties of a molecular junction. Constructive interference (green line) in a symmetric molecule would results in a continuous transmission function. This smooth change (low slope) would generate a low Seebeck coefficient. Destructive interference (red line) near the Fermi level in an asymmetric molecule results in a noticeable dip in the transmission. This significant changes in the transmission (high slope) would generate a high Seebeck coefficient. (c) SEM image of a 2D array of gold nanoparticles.

In this paper, we investigate the effect of DQI in molecular junctions on the thermoelectric properties of hybrid NPA monolayers consisting of molecules and Au nanoparticles. In particular, we measure the Seebeck coefficient and power factor of

monolayers of 1,3-benzenedithiol (1,3-BDT) capped gold nanoparticles and 1,4-benzenedithiol (1,4-BDT) capped gold nanoparticles (Figure 1). The difference between these two molecules is that the sulfur atoms are in different positions in benzene rings resulting in a symmetric configuration for 1,4-BDT (para) and an asymmetric configuration for 1,3-BDT (meta). The symmetric and asymmetric configurations provide distinctly different energy-dependent transmission functions. In particular, in the meta case sharp dips appear due to the phase difference of the charge carrier through the two paths around the molecule resulting in DQI. The quantum interference node results in significantly higher slopes in the transmission, which results in higher Seebeck coefficients [52].

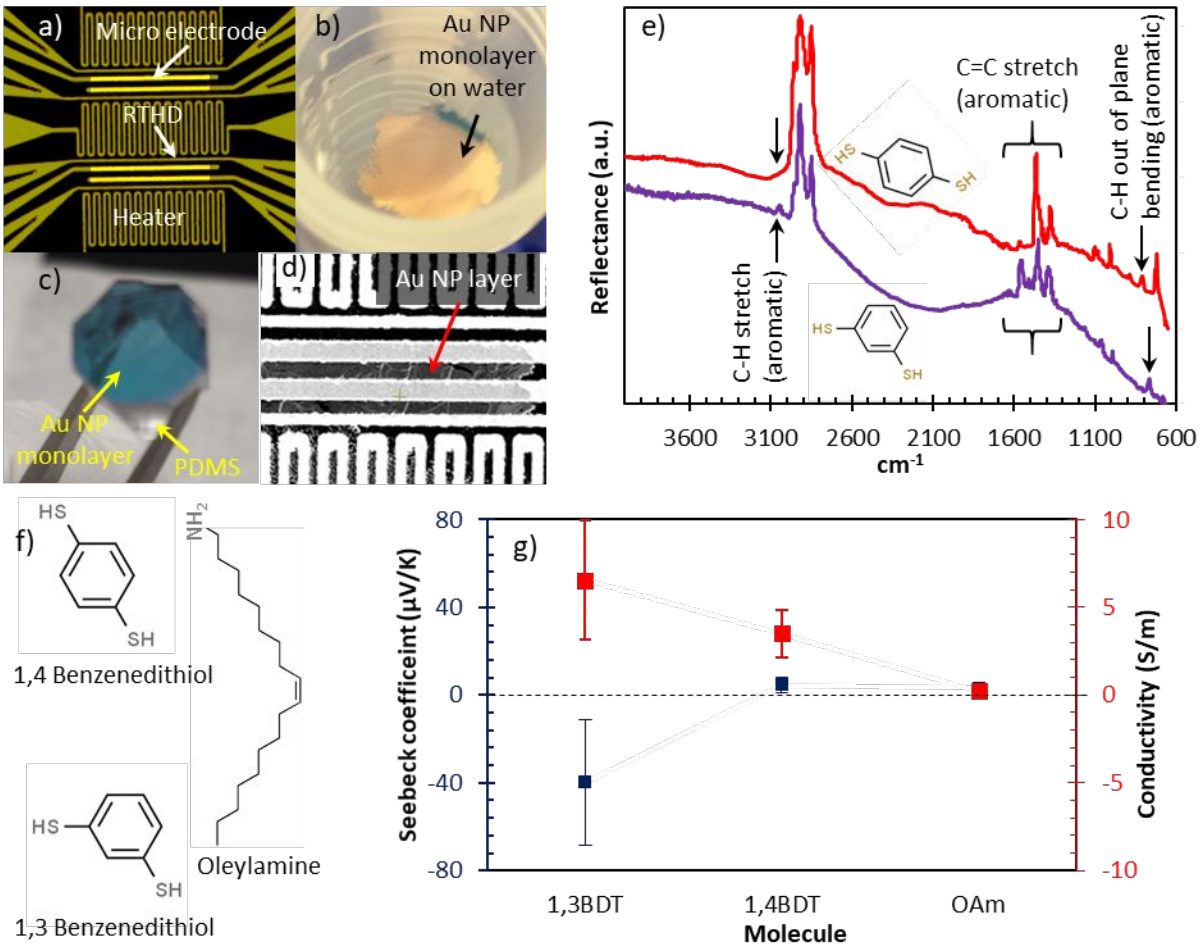

Figure 2. Thermoelectric measurements of hybrid molecule-nanoparticle monolayers. (a) Optical image of thermoelectric chip consisting of heaters, resistance thermometer devices (RTHDs), and microelectrodes providing a suitable platform for measuring the Seebeck coefficient; (b) formation of a monolayer of oleylamine capped gold nanoparticles on the surface of the water; (c) Monolayer transferred to the surface of a PDMS stamp. (d) SEM image of the stamped monolayer on a thermoelectric chip in the open area around the microelectrodes; (e) FTIR spectroscopy of 1,3 BDT-Au NPs (purple) and 1,4BDT-Au NPs (red) showing the presence of the BDT molecules after the ligand exchange process; (f) molecular structure of 1,4 BDT, 1,3 BDT, and oleylamine. (g) Seebeck coefficient (blue) and conductivity (red) of the monolayers.

Results and discussion

The details of the Seebeck coefficient and conductivity measurement procedures are described in a previous work [13]. The optical image of thermoelectric chip used for taking the measurements is shown in Figure 2(a). The chip is fabricated using standard photolithography processes and includes resistive heaters to create a thermal gradient,

resistance thermometer devices (RTHDs) for measuring the temperature gradient across the device and calibrating the heater, and pairs of microelectrodes for measuring the generated thermoelectric voltage and device conductivity. The surface of the chip is covered with a thin silicon nitride insulator layer except for the area between and around the microelectrodes. This opening allows electrical connection to the deposited materials through the microelectrodes for measurement purposes while the rest of the chip remains isolated. An instrumentation amplifier is used to measure the generated thermoelectric voltage across two microelectrodes.

For characterizing the effect of the different isomers of BDT on the thermoelectric performance, we first deposit a 2D monolayer of gold nanoparticles on the surface of the thermoelectric chip. The gold nanoparticles are initially covered with oleylamine due to the synthesis process [55]. The deposition process starts with the formation of self-assembly of a monolayer of oleylamine capped gold nanoparticles on the surface of the water, shown in Figure 2(b), followed by a microcontact transfer process using a small Polydimethylsiloxane (PDMS) stamp to place the layer on to a thermoelectric chip, as shown in Figure 2(c). Figure 2(d) shows an SEM image of the oleylamine capped gold monolayer deposited on the insulation-free opening section of the chip. Oleylamine, shown in Figure 2(f), is a long chain molecule and acts as an insulation layer in between nanoparticles. After deposition, the long oleylamine chain can be replaced with either 1,3BDT or 1,4BDT, shown in Figure 2(f), using a solid-state ligand exchange process [49, 56]. The solid-state ligand exchange process was performed by immersing the entire chip into the 1,3 BDT or 1,4 BDT solution (0.1% by volume in acetonitrile) overnight and then rinsing three times with the same fresh solution. Figure 2(e) shows the Fourier transform

infrared spectroscopy (FTIR) spectra of 1,3 BDT and 1,4 BDT capped gold nanoparticles. To investigate the presence of benzenedithiol on the surface of the Au NPs after the ligand exchange process, we monitored the aromatic peaks at FTIR spectra of both samples with 1,3BDT and 1,4BDT capped gold nanocrystals. The peaks associated to the aromatic C-H out of plane bending at 780 cm^{-1} and 800 cm^{-1} for 1,3 BDT-Au NPs and 1,4 BDT-Au-NPs as well as aromatic C-H stretch at 3060 cm^{-1} for both samples signify the existance of BDT on the surface of the Au NPs. Moreover, FTIR shows further evidence of BDT with three aromatic peaks of C=C stretch in the spectrum range of 1380 cm^{-1} and 1600 cm^{-1}. The absence of amine N-H stretch peaks between 3300-3500 cm^{-1} indicates efficient removal of oleylamine during the ligand exchange process. The sulfur atoms on the BDT provide a strong coupling to the Au nanoparticles ensuring the presence of the ligand for a long time and its stability during the Seebeck coefficient measurements.

To measure the Seebeck coefficient, a thermal gradient ranging between 0 and 0.6 K is applied across the molecule-Au monolayer by applying DC voltage to one of the heaters. This in turn generates a thermovoltage which is used to calculate the Seebeck coefficient for each device based on the applied thermal gradient. The Seebeck coefficients extracted for each monolayer are presented in Figure 2(g). The Seebeck coefficient for native hybrid films (monolayer of oleylamine capped Au nanoparticles) is a low positive number (S = 3.36 μV/K) indicating p-type (HOMO-dominated) transport, and the resulting conductivity is σ = 0.21 S/m. After replacing the oleylamine ligand with 1,4 BDT, the conductivity of the monolayer increases by more than 16 times to σ = 3.5 S/m. This conductivity improvement is another indicator of the success of the ligand exchange

process. The electric conductivity is greatly affected by the exchange to 1,4 BDT, but the corresponding change in the Seebeck coefficient is smaller, with a 42% improvement (S = 4.77 μV/K). The positive Seebeck coefficient indicates p-type transport and the major contribution of holes in the conduction process of the thin film.

However, the observed behavior for the 1,3 BDT monolayers is strikingly different. Replacing the oleylamine ligand with 1,3 BDT changes the sign of the Seebeck coefficient from positive to negative, indicating a change in the transport to n-type with electrons dominating the conduction process. The magnitude of the Seebeck coefficient increased at least by a factor of 4.2 reaching S=-14.2 μV/K and at most by a factor of 30 reaching S=-102.7 μV/K. Moreover, the electric conductivity measurement shows maximum 55-fold improvement to σ=11.73 S/m and minimum 12-fold improvement to σ=2.5 S/m. The simultaneous improvement of both the Seebeck coefficient and the electrical conductivity demonstrate the importance of details of the electronic structure of the molecule on the overall film properties. We should note that the major source of error in the measurements for BDT molecules is the result of the ligand exchange process [48]. Since the size of the BDT molecule is much smaller than OAM, the ligand exchange process degrades the quality of the layer by dislocating the Au NPs and introducing cracks to the monolayer.

To understand the change in the dominant charge carrier and the conductance for these systems it is useful to determine the location of the relevant energy levels for both the 1,3BDT-Au and 1,4BDT-Au NP arrays. To achieve this, ultraviolet photoelectron spectroscopy (UPS) and UV-VIS-NIR spectroscopy are utilized. Figure 3(a) and (b) present the energetics from the UPS spectrum of 60-nm-thick films made of 1,3BDT-Au NPs and 1,4BDT-Au NPs on a silicon substrate. The high binding energy cut-off, shown

in Figure 3(a), reveals that the work functions of the 1,3BDT-Au and 1,4BDT-Au films are $\Phi_{1,3BDT}$ = 4.43 eV and $\Phi_{1,4BDT}$ = 4.87 eV, respectively. The low binding energy measurement, shown in Figure 3(b), disclose that HOMO energy of 1,3BDT-Au NPs and 1,4BDT-Au NPs are located at $E_{HOMO,1,3BDT}$ = −5.81 eV and at $E_{HOMO,1,4BDT}$ = −6.22 eV, respectively. To determine the LUMO level, we measured optical band gap energy of a thin layer deposited on a glass substrate. Figure 3(c) shows the UV-VIS-NIR absorption spectra of 1,3BDT-Au NPs and 1,4BDT-Au NPs samples. The optical bandgap energy of 1,3BDT-Au NPs and 1,4BDT-Au NPs are 4.38 eV and 4.42 eV, respectively. Therefore, LUMO energy is located at −1.43 eV for 1,3BDT-Au NPs and −1.8 eV for 1,4BDT-Au NPs. The energy levels, shown in Figure 3(d), demonstrate that the bandgap and the relative position of the Fermi level with respect to the HOMO for both type samples are similar. Interestingly, although the measured Fermi level of both samples are closer to HOMO rather than LUMO, the measured Seebeck coefficient in 1,3BDT-Au NPs sample is much larger, and negative rather than positive.

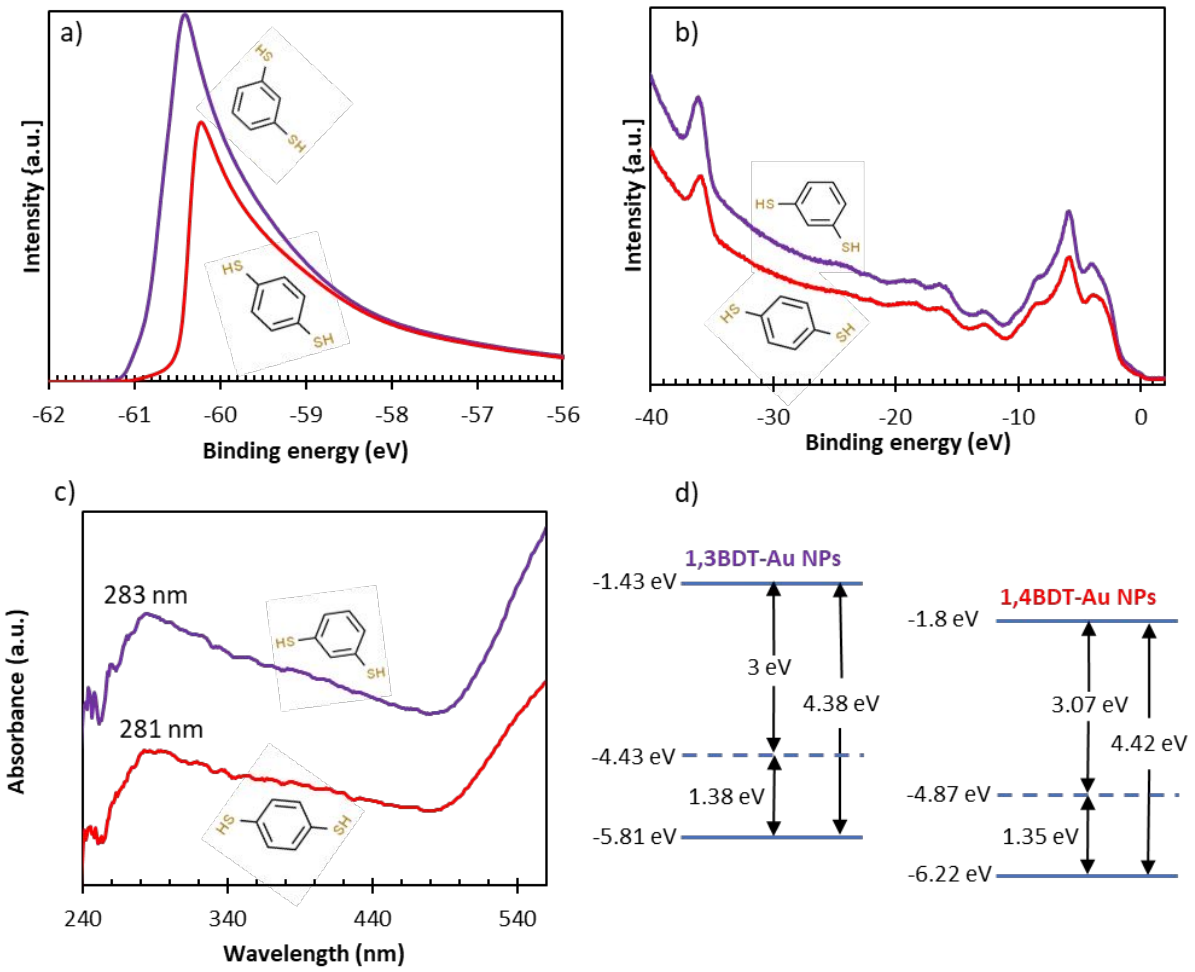

Figure 3. spectroscopy results of 60-nm-thick hybrid molecule-Au NPs thin film. (a) ultraviolet photoelectron high-binding-energy cutoff spectra for 1,3BDT-capped Au NPs film (purple) and for 1,4BDT-capped Au NPs film (red) on a silicon substrate used for work function calculation; (b) ultraviolet photoelectron low-binding-energy cutoff spectra for 1,3BDT-capped Au NPs film (purple) and 1,4BDT-capped Au NPs film (red) on a silicon substrate used for energy difference between valence band and Fermi level calculation; (c) optical absorption spectrum of a thin film of 1,3BDT-capped Au NPs (purple), 1,4BDT-capped Au NPs (red); (d) Energy level diagram of 1,3BDT-capped Au NPs and 1,4BDT-capped Au NPs. The first excitonic absorption for each material is used to determine optical bandgap (Eg = 4.38 eV for 1,3BDT-capped Au NPs and Eg = 4.42 eV for 1,4BDT-capped Au NPs).

Beyond the Seebeck coefficient, the most important parameter for thermoelectric materials is the efficiency. And, although the overall efficiency requires knowledge of the electrical conductivity, thermal conductivity, and Seebeck coefficient, the numerator in the expression for ZT (σS^2), referred to as the power factor, is often used as a first-order proxy for comparing the effective improvements of comparable systems and providing

insights into the performance of thermoelectric devices. Because thermal conductivity measurement is a challenging task for nanoparticle systems [22, 57, 58], the power factor is frequently reported as an indicator of the performance of thermoelectric devices [8, 35, 48]. The mean value of the power factor for all three samples is shown in the inset of Figure 4(a). Replacing oleylamine with 1,4BDT improves the power factor for more than 50 times from 2.67 pW/m.K^2 for oleylamine-Au NPs film to 142 pW/m.K^2 for 1,4BDT-Au NPs film. This improvement comes mostly from the increase in the conductivity in the BDT film. However, by replacing the oleylamine with 1,3BDT both the conductivity and the Seebeck coefficient are enhanced leading to significant improvement in the power factor. The power factor increases from 2.67 ± 0.85 pW/m.K2 for oleylamine-Au NP films to 21.3 ± 13.5 nW/m.K2 for 1,3BDT-Au NP films. The minimum improvement for all samples was 340 times better for the 1,3BDT. In addition, comparison between 1,3BDT-Au and 1,4BDT-Au NP films shows that although the conductance is similar in both cases, the power factor of the 1,3BDT-Au NP thin film is at least ~4 times higher than that of the 1,4BDT-Au NPs thin film (comparing the poorest and best performing devices, respectively), and the average improvement across all samples is 150 ± 94.9. All uncertainty values are given by the standard error of the mean. A drastic increase in performance with the small change in the isomeric formulation of the molecules.

The I-V characteristic, as shown in Figure 4(c), is used to measure the conductance of the device for the power factor calculations. The current is measured over +/-0.2 V range, and the I-V is linear over this range.

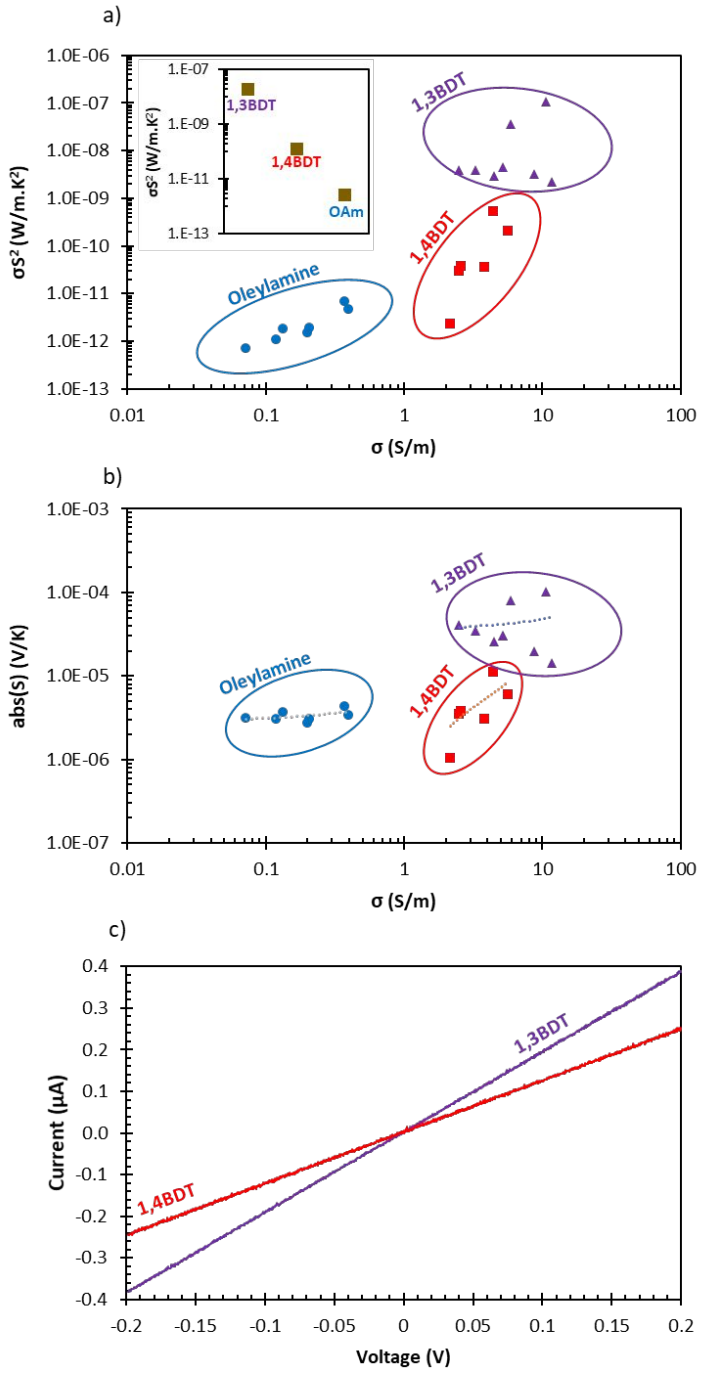

Figure 4. experimental results. (a) power factor as a function of conductivity; (b) Seebeck coefficient as a function of conductivity; (c) I-V characteristics of the monolayers.

To understand this range of observed phenomena we first note that in the case of NPAs, where the individual nanoparticles can be considered essentially isothermal, it has been established that $S_{NPA} \approx S_{junction}$ [8, 13, 35]. And, as shown in Equation (2), the

Seebeck coefficient in a molecular junction is proportional to the slope of the transmission function when a charge carrier is tunneling between the particles. As such, the observed behavior of our NPA systems must be attributed to the transmission properties of organic linkers in the hybrid array. To that end, we reiterate that the asymmetric contact configuration in 1,3-BDT results in DQI which yields nodes in the transmission plot [59-61] as shown in the in Fig. 1b (red), while the symmetric contacts in 1,4BDT results in constructive interference, and the transmission plot is continuous between the HOMO and LUMO levels [60, 61] (Fig. 1b, green). The presence of DQI in the transmission function yields several effects that provide insights into our experimental results. First, the significant differences in slope between the DQI case and the non-DQI case result in a significantly higher Seebeck coefficient for 1,3BDT. Secondly, we note that the position of the node in the DQI case is located closer to the HOMO level than the LUMO level indicating the possibility of observing a negative Seebeck coefficient even when the Fermi energy of the system is closer to the HOMO level. More precisely, this indicates that the large negative Seebeck coefficient observed for 1,3BDT indicates that the Fermi level is located on the rising edge of the node in the transmission plot. And third, there can be a wide range of values where the transmission probability in the DQI case is higher than, or at least similar to, the non-DQI case [60, 61] as shown schematically in Fig. 1b, thus resulting in potentially similar conductance values for the two films. This implies that in nanoscale thermoelectric devices, using DQI can allow simultaneous improvements of both the conductance and Seebeck coefficient of the system, greatly improving the overall power factor of the system. Thus, all of our experimental observations can be attributed

to the presence of a DQI node near the Fermi level that arises due to the asymmetric structure of the 1,3BDT molecule.

Although a lower conductance is generally anticipated for molecules showing a DQI effect [62, 63], the location of the Fermi level and the linker chemistry have significant effects on the conductance of the molecular junction [60, 61, 64, 65]. For single-molecule conductance measurements 1,3BDT and 1,4BDT have been reported to have similar conductance values of 0.004 ±0.001 G0 and 0.005 ±0.001 G0 respectively. These differences are much smaller than the differences reported for similar molecules with amine anchoring groups (0.005 ±0.001 G0 for 1,3-benzenediamine and 0.01 ±0.003 G0 for 1,4-benzenediamine) [66]. In addition, in the case of nanoparticles, the Fermi energy is sensitive to the binding of molecules and their anchoring groups [67-69]. Thus, the ~2x improvement in the conductance of the 1,3BDT array may stem from the nanoparticle Fermi energy alignment with the molecular junction.

Nanoparticle concentration is another factor that may affect the thermoelectric properties of the hybrid molecule-NP structures. Since a monolayer of a superlattice of molecule-Au NPs is deposited on the TEC chip, a higher concentration Au NPs is attributed to the smaller size Au NPs. As long as the size of nanoparticles are large enough to be beyond the coulomb-blockade threshold, their size (e.g. concentration) should have little impact on thermoelectric values of the system. In general, if the Seebeck coefficient for a molecular junction is much greater than the Seebeck coefficient for the nanoparticles in the array, then it is expected that $S_{NPA} \approx S_{JUNCTION}$ [8, 35].

Conclusion and outlook

In summary, we investigate the effect of molecular-scale, DQI on the thermoelectric performance of BDT-Au, 2D monolayers. In this study, we used symmetric (para configuration, 1,4BDT) and asymmetric BDT structures (meta configuration, 1,3BDT) to show that quantum interference in the meta configuration can significantly enhance the overall thermoelectric performance of the device and simultaneously drive increases in both the electrical conductance and the Seebeck coefficient. The small, isomeric change that occurs from the movement of a single substituent group in the interlinkers resulted in an improvement of the power factor. The results show promising opportunities for the design of high efficiency thermoelectric devices based on quantum interference effects in nanoscale systems.

Experimental section

Nanoparticle synthesis

Inside the glovebox at inert condition, ~15 nm Au nanoparticles were synthesized by rapidly injecting a solution of 150 mg of tetrachloroauric acid (HAuCl4) in 3.6 mL of technical grade oleylamine and 3.0 mL of toluene into a boiling solution of 8.7 mL of technical grade oleylamine in 147 mL of toluene. The color of the solution changed to bright yellow and then gradually to deep red. Heating is stopped after 2 hours and 450 mL of methanol was added to precipitate the product. The particles were isolated by centrifugation and washed at least two times to remove unreacted starting materials and biproducts. Washing process involves dispersion in Toluene via vortex and precipitation in methanol via centrifuge.

Thermoelectric chip fabrication process

The fabrication process started with a cleaning the silicon covered with nitride wafer. Then 1μm-thick positive photoresist (S1813) was spin-coated on the wafer. Subsequently, after soft baking, the wafer was exposed to the UV light to define the required pattern. The process was continued by a brief soft baking and then developing in MF CD-26. Then Si3N4 layer at defined areas was etched for 50nm with ICP etching method followed by 5/40-nm-thick Cr/Au metals metal deposition and lift-off processes. In order to have a correct measurement, all the connections on the chip are required to be coated with an isolating layer and only microelectrodes should be exposed to the monolayer. Therefore, 100-nm thick silicon nitride (Si3N4) was deposited on the whole surface of the chip with PECVD method. Similar to the first layer process, standard photolithography method and etching process were utilized to define opening areas and remove Si_3N_4 at that areas.

Monolayer preparation method

To perform the monolayer self-assembly, the prepared Au nanoparticle solution was diluted with toluene in a 1:4 (Au NP:toluene) ratio to make a working solution. Next, for each nano particle array, 12 mL of distilled water was poured in a 14 mL centrifuge tube and placed in the fume hood. Then, 250 µL of working solution was deposited onto the surface of the distilled water. The monolayer was formed in less than 4 hours. After that, a cube of polymethyldisiloxane (PDMS) was pushed through the surface of the distilled water to extract the Au arrays. The process followed by lightly spraying the cube with N2 to remove any excess air bubbles on the surface. Finally, the surface of the PDMS stamp with the array was carefully rolled over the surface of the thermoelectric chip to transfer the Au nano particle array to the chip.

Thermoelectric measurement process

An on-chip resistive heater generated a thermal gradient, and on-chip resistance thermometer devices (RTHDs) were used to calibrate the temperature difference (ΔT). In the calibration process, RTHDs are used to calculate the temperature gradient on the device as a function of the voltage applied to the adjacent heaters. Then during the Seebeck coefficient measurement, a voltage is applied to one of the heaters and the generated voltage levels across the microelectrodes of the adjacent device are measured. A differential instrumentation amplifier measured the thermovoltage (ΔV) across the microelectrodes and based on these data the Seebeck coefficient ($S=-\Delta V/\Delta T$) is calculated for each measurement. A range of thermal gradients between 0 to 0.6K was applied to microelectrodes allowing the extraction of the Seebeck coefficient from a plot of ΔV vs ΔT.

Energy level calculations

UPS provides a measure of the energy distribution of occupied states. High binding energy cut-off of the UPS spectrum referenced to E_F=0 eV is shown in Figure 3(a). The cut-off energy of the secondary electron determines from the data presented by the intersection of the linear extrapolation of the cut-off region and the binding energy axis. This is located at binding energy of E_g = -60.92 eV for 1,3BDT-Au NPs and E_g = -60.48 eV for 1,4BDT-Au NPs resulting the work function of $\Phi_{1,3BDT}$ = hυ - 60.92= 4.43 eV for 1,3BDT-Au NPs and $\Phi_{1,4BDT}$ = hυ - 60.48 = 4.87 eV for 1,4BDT-Au NPA. The low binding energy measurement of the HOMO energy is shown in Figure 3(b). HOMO also referenced to E_F= 0 eV was defined by the data provided from the intersection of the base line to the linear extrapolation of the cut-off region. The intersections are located at 1.38 eV for 1,3BDT-Au NPs and at 1.35 eV for 1,4BDT-Au NPs relating to the distance between the Fermi level and the HOMO. When referenced to the vacuum level (E_{vac}= 0) HOMO energy is located at $E_{HOMO,1,3BDT}$ = −5.81 eV for 1,3BDT-Au NPs and at $E_{HOMO,1,4BDT}$ = −6.22 eV for 1,4BDT-Au NPs. The energy of the LUMO, approximates the sum of the HOMO energy level and optical bandgap energy. Optical band gap energy is measured with UV-VIS-NIR spectroscopy on a thin layer of samples on glass substrate. The optical bandgap energy equals E_g= 1.92 eV for 1,3BDT-Au NPs and E_g= 1.96 eV for 1,4BDT-Au NPs. Therefore, LUMO energy is located at $E_{LUMO,1,3BDT}$ = −3.89 eV for 1,3BDT-Au NPs and at $E_{HOMO,1,4BDT}$ = −4.26 eV for 1,4BDT-Au NPs.

UV–VIS-NIR measurement

Optical absorption measurements were carried out in a Shimadzu UV/Vis/NIR Spectrophotometer (350–1200 nm) at Center for Advanced Microstructures and Devices

(CAMD) at Louisiana State University (LSU). Multiple layers of Au nanoparticles were spin coated on soda lime glass substrate. For 1,3BDT-Au NPs and 1,4BDT-Au NPs, the layer-by-layer ligand exchange process was performed as described in the text.

Fourier Transform Infrared spectroscopy (FTIR) measurement

FTIR measurement was carried at the infrared micro spectroscopy endstation at the CAMD synchrotron facility of LSU. The Thermo Nicolet Nexus 670 FT-IR spectrometer was used to collect the IR spectra of the samples. The spectrometer is equipped with a DTGS detector and a Globar source. The sample was prepared by multiple spin coating oleylamine-Au NPs on a clean gold-coated mica substrate. After depositing each layer, ligand exchange process was performed as described before to replace oleyalmine with 1,3BDT or 1,4BDT depending on the required molecule. The IR reflection spectra were acquired with 45° incident angle by using VeeMaxII Variable Angle Specular Reflectance box.

Ultraviolet photoelectron spectroscopy (UPS) measurement

UPS measurement was carried at the 5-meter toroidal grating monochromator (5m-TGM) beamline at CAMD at LSU. The beamline is furnished with a photoemission endstation using an Omicron EA125 hemispherical electron energy analyzer with five channel detector and dual Mg/Al X-ray source. UPS measurements were acquired in an ultra-high vacuum chamber (pressure of 10^{-10} mbar) with a constant pass energy of 10 eV, at a photon energy of 65.35 eV. All UPS spectra were collected in normal emission geometry with a 45° incident angle to the surface normal. The binding energies are referenced with gold Fermi level which is in electrical contact with the sample. The samples were 60-nm-thick films made of 1,3BDT-Au NPs and 1,4BDT Au NPs on a 10 mm × 10 mm silicon

substrate. High binding energy cut-off measurement was performed while the sample was biased at −10.0 V to split the secondary edges of the analyzer.

Acknowledgments

The authors acknowledge financial support from the US NSF (CBET-1605338, ECCS-1807555, and ECCS- 2036865).

References

[1] L. E. Bell, "Cooling, heating, generating power, and recovering waste heat with thermoelectric systems," *Science,* vol. 321, no. 5895, pp. 1457-1461, 2008.

[2] P. D. Mitcheson, "Energy harvesting for human wearable and implantable bio-sensors," in *2010 Annual International Conference of the IEEE Engineering in Medicine and Biology*, 2010: IEEE, pp. 3432-3436.

[3] S. Gong and W. Cheng, "Toward soft skin-like wearable and implantable energy devices," *Advanced Energy Materials,* vol. 7, no. 23, p. 1700648, 2017.

[4] T. Ghomian and S. Mehraeen, "Survey of energy scavenging for wearable and implantable devices," *Energy,* vol. 178, pp. 33-49, 2019.

[5] G. L. Wilcox and G. J. Giesler Jr, "An instrument using a multiple layer Peltier device to change skin temperature rapidly," *Brain research bulletin,* vol. 12, no. 1, pp. 143-146, 1984.

[6] S. M. Lindsay, "Variable temperature scanning probe microscope based on a peltier device," ed: Google Patents, 1997.

[7] Y. Yan and J. A. Malen, "Periodic heating amplifies the efficiency of thermoelectric energy conversion," *Energy & Environmental Science,* vol. 6, no. 4, pp. 1267-1273, 2013.

[8] W. Chang, B. Russ, V. Ho, J. Urban, and R. Segalman, "Gold nanocrystal arrays as a macroscopic platform for molecular junction thermoelectrics," *Physical Chemistry Chemical Physics,* vol. 17, no. 9, pp. 6207-6211, 2015.

[9] H. Zhang, J. S. Son, J. Jang, J.-S. Lee, W.-L. Ong, J. A. Malen, and D. V. Talapin, "Bi1–x Sb x Alloy Nanocrystals: Colloidal Synthesis, Charge Transport, and Thermoelectric Properties," *Acs Nano,* vol. 7, no. 11, pp. 10296-10306, 2013.

[10] K. Wang, E. Meyhofer, and P. Reddy, "Thermal and thermoelectric properties of molecular junctions," *Advanced Functional Materials,* vol. 30, no. 8, p. 1904534, 2020.

[11] J. J. Urban, A. K. Menon, Z. Tian, A. Jain, and K. Hippalgaonkar, "New horizons in thermoelectric materials: Correlated electrons, organic transport, machine learning, and more," *Journal of Applied Physics,* vol. 125, no. 18, p. 180902, 2019.

[12] M. S. Dresselhaus, G. Chen, M. Y. Tang, R. Yang, H. Lee, D. Wang, Z. Ren, J. P. Fleurial, and P. Gogna, "New directions for low-dimensional thermoelectric materials," *Advanced materials,* vol. 19, no. 8, pp. 1043-1053, 2007.

[13] C. E. McCold, L. Domulevicz, Z. Cai, W.-Y. Lo, S. Hihath, K. March, H. M. Mohammad, M. Anantram, L. Yu *et al.*, "Molecular Control of Charge Carrier and Seebeck Coefficient in Hybrid Two-Dimensional Nanoparticle Superlattices," *The Journal of Physical Chemistry C,* vol. 124, no. 1, pp. 17-24, 2019.

[14] A. Majumdar and P. Reddy, "Role of electron–phonon coupling in thermal conductance of metal–nonmetal interfaces," *Applied Physics Letters,* vol. 84, no. 23, pp. 4768-4770, 2004.
[15] T. Harman, P. Taylor, M. Walsh, and B. LaForge, "Quantum dot superlattice thermoelectric materials and devices," *science,* vol. 297, no. 5590, pp. 2229-2232, 2002.
[16] A. I. Hochbaum, R. Chen, R. D. Delgado, W. Liang, E. C. Garnett, M. Najarian, A. Majumdar, and P. Yang, "Enhanced thermoelectric performance of rough silicon nanowires," *Nature,* vol. 451, no. 7175, pp. 163-167, 2008.
[17] S. Yee, J. Malen, P. Reddy, R. Segalman, and A. Majumdar, "Thermoelectricity at the organic-inorganic interface," in *International Heat Transfer Conference*, 2010, vol. 49392, pp. 845-855.
[18] L. Cui, S. Hur, Z. A. Akbar, J. C. Klöckner, W. Jeong, F. Pauly, S.-Y. Jang, P. Reddy, and E. Meyhofer, "Thermal conductance of single-molecule junctions," *Nature,* vol. 572, no. 7771, pp. 628-633, 2019.
[19] D. G. Cahill, W. K. Ford, K. E. Goodson, G. D. Mahan, A. Majumdar, H. J. Maris, R. Merlin, and S. R. Phillpot, "Nanoscale thermal transport," *Journal of applied physics,* vol. 93, no. 2, pp. 793-818, 2003.
[20] D. G. Cahill, P. V. Braun, G. Chen, D. R. Clarke, S. Fan, K. E. Goodson, P. Keblinski, W. P. King, G. D. Mahan *et al.*, "Nanoscale thermal transport. II. 2003–2012," *Applied physics reviews,* vol. 1, no. 1, p. 011305, 2014.
[21] P. Reddy, S.-Y. Jang, R. A. Segalman, and A. Majumdar, "Thermoelectricity in molecular junctions," *Science,* vol. 315, no. 5818, pp. 1568-1571, 2007.
[22] J. A. Malen, S. K. Yee, A. Majumdar, and R. A. Segalman, "Fundamentals of energy transport, energy conversion, and thermal properties in organic–inorganic heterojunctions," *Chemical Physics Letters,* vol. 491, no. 4-6, pp. 109-122, 2010.
[23] C. Meng, C. Liu, and S. Fan, "A promising approach to enhanced thermoelectric properties using carbon nanotube networks," *Advanced Materials,* vol. 22, no. 4, pp. 535-539, 2010.
[24] T. Humphrey, M. O'Dwyer, and H. Linke, "Power optimization in thermionic devices," *Journal of Physics D: Applied Physics,* vol. 38, no. 12, p. 2051, 2005.
[25] D. M. Rowe, *CRC handbook of thermoelectrics*. CRC press, 2018.
[26] C. Joachim and S. Roth, *Atomic and molecular wires*. Springer Science & Business Media, 1997.
[27] M. Bürkle, L. Xiang, G. Li, A. Rostamian, T. Hines, S. Guo, G. Zhou, N. Tao, and Y. Asai, "The orbital selection rule for molecular conductance as manifested in tetraphenyl-based molecular junctions," *Journal of the American Chemical Society,* vol. 139, no. 8, pp. 2989-2993, 2017.
[28] L. Xiang, T. Hines, J. L. Palma, X. Lu, V. Mujica, M. A. Ratner, G. Zhou, and N. Tao, "Non-exponential length dependence of conductance in iodide-terminated oligothiophene single-molecule tunneling junctions," *Journal of the American Chemical Society,* vol. 138, no. 2, pp. 679-687, 2016.
[29] S. Guo, G. Zhou, and N. Tao, "Single molecule conductance, thermopower, and transition voltage," *Nano letters,* vol. 13, no. 9, pp. 4326-4332, 2013.
[30] I. Diez-Perez, J. Hihath, T. Hines, Z.-S. Wang, G. Zhou, K. Müllen, and N. Tao, "Controlling single-molecule conductance through lateral coupling of π orbitals," *Nature nanotechnology,* vol. 6, no. 4, pp. 226-231, 2011.
[31] L. Venkataraman, J. E. Klare, C. Nuckolls, M. S. Hybertsen, and M. L. Steigerwald, "Dependence of single-molecule junction conductance on molecular conformation," *Nature,* vol. 442, no. 7105, pp. 904-907, 2006.
[32] J. E. Greenwald, J. Cameron, N. J. Findlay, T. Fu, S. Gunasekaran, P. J. Skabara, and L. Venkataraman, "Highly nonlinear transport across single-molecule junctions via destructive quantum interference," *Nature Nanotechnology,* vol. 16, no. 3, pp. 313-317, 2021.

[33] M. H. Garner, H. Li, Y. Chen, T. A. Su, Z. Shangguan, D. W. Paley, T. Liu, F. Ng, H. Li *et al.*, "Comprehensive suppression of single-molecule conductance using destructive σ-interference," *Nature,* vol. 558, no. 7710, pp. 415-419, 2018.

[34] M. Kamenetska, J. Widawsky, M. Dell'Angela, M. Frei, and L. Venkataraman, "Temperature dependent tunneling conductance of single molecule junctions," *The Journal of Chemical Physics,* vol. 146, no. 9, p. 092311, 2017.

[35] K.-H. Müller, "Thermoelectrics in an array of molecular junctions," *The Journal of chemical physics,* vol. 129, no. 4, p. 044708, 2008.

[36] C. R. Arroyo, S. Tarkuc, R. Frisenda, J. S. Seldenthuis, C. H. Woerde, R. Eelkema, F. C. Grozema, and H. S. Van Der Zant, "Signatures of quantum interference effects on charge transport through a single benzene ring," *Angewandte Chemie International Edition,* vol. 52, no. 11, pp. 3152-3155, 2013.

[37] T. Hansen, G. C. Solomon, D. Q. Andrews, and M. A. Ratner, "Interfering pathways in benzene: An analytical treatment," *The Journal of chemical physics,* vol. 131, no. 19, p. 194704, 2009.

[38] G. Yang, H. Wu, J. Wei, J. Zheng, Z. Chen, J. Liu, J. Shi, Y. Yang, and W. Hong, "Quantum interference effect in the charge transport through single-molecule benzene dithiol junction at room temperature: An experimental investigation," *Chinese Chemical Letters,* vol. 29, no. 1, pp. 147-150, 2018.

[39] P. Gehring, J. M. Thijssen, and H. S. van der Zant, "Single-molecule quantum-transport phenomena in break junctions," *Nature Reviews Physics,* vol. 1, no. 6, pp. 381-396, 2019.

[40] M. T. Lusk, C. A. Stafford, J. D. Zimmerman, and L. D. Carr, "Control of exciton transport using quantum interference," *Physical Review B,* vol. 92, no. 24, p. 241112, 2015.

[41] J. P. Bergfield, G. C. Solomon, C. A. Stafford, and M. A. Ratner, "Novel quantum interference effects in transport through molecular radicals," *Nano letters,* vol. 11, no. 7, pp. 2759-2764, 2011.

[42] C. A. Stafford, D. M. Cardamone, and S. Mazumdar, "The quantum interference effect transistor," *Nanotechnology,* vol. 18, no. 42, p. 424014, 2007.

[43] S.-H. Ke, W. Yang, and H. U. Baranger, "Quantum-interference-controlled molecular electronics," *Nano letters,* vol. 8, no. 10, pp. 3257-3261, 2008.

[44] G. C. Solomon, D. Q. Andrews, T. Hansen, R. H. Goldsmith, M. R. Wasielewski, R. P. Van Duyne, and M. A. Ratner, "Understanding quantum interference in coherent molecular conduction," *The Journal of chemical physics,* vol. 129, no. 5, p. 054701, 2008.

[45] S. Yaliraki, M. Kemp, and M. A. Ratner, "Conductance of Molecular Wires: Influence of Molecule− Electrode Binding," *Journal of the American Chemical Society,* vol. 121, no. 14, pp. 3428-3434, 1999.

[46] V. J. Langlais, R. R. Schlittler, H. Tang, A. Gourdon, C. Joachim, and J. Gimzewski, "Spatially resolved tunneling along a molecular wire," *Physical review letters,* vol. 83, no. 14, p. 2809, 1999.

[47] M. Magoga and C. Joachim, "Conductance and transparence of long molecular wires," *Physical Review B,* vol. 56, no. 8, p. 4722, 1997.

[48] C. E. McCold, Q. Fu, J. Y. Howe, and J. Hihath, "Conductance based characterization of structure and hopping site density in 2D molecule-nanoparticle arrays," *Nanoscale,* vol. 7, no. 36, pp. 14937-14945, 2015.

[49] T. Ghomian, O. Kizilkaya, and J.-W. Choi, "Lead sulfide colloidal quantum dot photovoltaic cell for energy harvesting from human body thermal radiation," *Applied energy,* vol. 230, pp. 761-768, 2018.

[50] T. Ghomian, S. Farimand, and J.-W. Choi, "The effect of isopropylamine-capped PbS quantum dots on infrared photodetectors and photovoltaics," *Microelectronic Engineering,* vol. 183, pp. 48-51, 2017.
[51] C. Evangeli, K. Gillemot, E. Leary, and M. Gonzalez, "R-Bollinger, G.; Lambert, C.; Agrait, N," *Nano Lett,* vol. 13, pp. 2141-2145, 2013.
[52] R. Miao, H. Xu, M. Skripnik, L. Cui, K. Wang, K. G. Pedersen, M. Leijnse, F. Pauly, K. Warnmark *et al.*, "Influence of quantum interference on the thermoelectric properties of molecular junctions," *Nano letters,* vol. 18, no. 9, pp. 5666-5672, 2018.
[53] M. Tsutsui, T. Morikawa, Y. He, A. Arima, and M. Taniguchi, "High thermopower of mechanically stretched single-molecule junctions," *Scientific reports,* vol. 5, p. 11519, 2015.
[54] J. Prasongkit and A. R. Rocha, "Quantum interference effects in biphenyl dithiol for gas detection," *RSC advances,* vol. 6, no. 64, pp. 59299-59304, 2016.
[55] H. Hiramatsu and F. E. Osterloh, "A simple large-scale synthesis of nearly monodisperse gold and silver nanoparticles with adjustable sizes and with exchangeable surfactants," *Chemistry of materials,* vol. 16, no. 13, pp. 2509-2511, 2004.
[56] C. E. McCold, Q. Fu, S. Hihath, J.-M. Han, Y. Halfon, R. Faller, K. van Benthem, L. Zang, and J. Hihath, "Ligand exchange based molecular doping in 2D hybrid molecule-nanoparticle arrays: length determines exchange efficiency and conductance," *Molecular Systems Design & Engineering,* vol. 2, no. 4, pp. 440-448, 2017.
[57] H. Babaei, M. E. DeCoster, M. Jeong, Z. M. Hassan, T. Islamoglu, H. Baumgart, A. J. McGaughey, E. Redel, O. K. Farha *et al.*, "Observation of reduced thermal conductivity in a metal-organic framework due to the presence of adsorbates," *Nature communications,* vol. 11, no. 1, pp. 1-8, 2020.
[58] S. Majumdar, J. A. Malen, and A. J. McGaughey, "Cooperative molecular behavior enhances the thermal conductance of binary self-assembled monolayer junctions," *Nano letters,* vol. 17, no. 1, pp. 220-227, 2017.
[59] L. A. Zotti and E. Leary, "Taming quantum interference in single molecule junctions: induction and resonance are key," *Physical Chemistry Chemical Physics,* vol. 22, no. 10, pp. 5638-5646, 2020.
[60] S. Gunasekaran, J. E. Greenwald, and L. Venkataraman, "Visualizing quantum interference in molecular junctions," *Nano letters,* vol. 20, no. 4, pp. 2843-2848, 2020.
[61] X. Li, Z. Tan, X. Huang, J. Bai, J. Liu, and W. Hong, "Experimental investigation of quantum interference in charge transport through molecular architectures," *Journal of Materials Chemistry C,* vol. 7, no. 41, pp. 12790-12808, 2019.
[62] D. Z. Manrique, C. Huang, M. Baghernejad, X. Zhao, O. A. Al-Owaedi, H. Sadeghi, V. Kaliginedi, W. Hong, M. Gulcur *et al.*, "A quantum circuit rule for interference effects in single-molecule electrical junctions," *Nature communications,* vol. 6, no. 1, pp. 1-8, 2015.
[63] M. Mayor, H. B. Weber, J. Reichert, M. Elbing, C. Von Hänisch, D. Beckmann, and M. Fischer, "Electric current through a molecular rod—relevance of the position of the anchor groups," *Angewandte Chemie International Edition,* vol. 42, no. 47, pp. 5834-5838, 2003.
[64] V. Tjoa, W. Jun, V. Dravid, S. Mhaisalkar, and N. Mathews, "Hybrid graphene–metal nanoparticle systems: electronic properties and gas interaction," *Journal of Materials Chemistry,* vol. 21, no. 39, pp. 15593-15599, 2011.
[65] P. Peljo, J. A. Manzanares, and H. H. Girault, "Contact potentials, fermi level equilibration, and surface charging," *Langmuir,* vol. 32, no. 23, pp. 5765-5775, 2016.
[66] M. Kiguchi, H. Nakamura, Y. Takahashi, T. Takahashi, and T. Ohto, "Effect of anchoring group position on formation and conductance of a single disubstituted benzene molecule bridging Au

electrodes: change of conductive molecular orbital and electron pathway," *The Journal of Physical Chemistry C,* vol. 114, no. 50, pp. 22254-22261, 2010.

[67] L. A. Zotti, T. Kirchner, J. C. Cuevas, F. Pauly, T. Huhn, E. Scheer, and A. Erbe, "Revealing the role of anchoring groups in the electrical conduction through single-molecule junctions," *small,* vol. 6, no. 14, pp. 1529-1535, 2010.

[68] F. Chen, X. Li, J. Hihath, Z. Huang, and N. Tao, "Effect of anchoring groups on single-molecule conductance: comparative study of thiol-, amine-, and carboxylic-acid-terminated molecules," *Journal of the American Chemical Society,* vol. 128, no. 49, pp. 15874-15881, 2006.

[69] A. Tan, J. Balachandran, S. Sadat, V. Gavini, B. D. Dunietz, S.-Y. Jang, and P. Reddy, "Effect of length and contact chemistry on the electronic structure and thermoelectric properties of molecular junctions," *Journal of the American Chemical Society,* vol. 133, no. 23, pp. 8838-8841, 2011.